Controller Design-oriented Analysis of Grid-forming Converters for Stability Robustness Enhancement

Yicheng Liao[1] *and Xiongfei Wang*[2*]

(1. School of Electrical Engineering and Computer Science, KTH Royal Institute of Technology, Stockholm 10044, Sweden;

2. AAU Energy, Aalborg University, Aalborg 9220, Denmark)

Abstract: Grid-forming converters can suffer from control interaction problems in grid connections that can result in small-signal instability. Their inner-loop voltage controller tends to interact with the outer-loop power controller, rendering the controller design more difficult. To conduct a design-oriented analysis, a control-loop decomposition approach for grid-forming converters is proposed. Combined with impedance-based stability analysis, the control-loop decomposition approach can reveal how different control loops affect the converter-grid interaction. This results in a robust controller design enabling grid-forming converters to operate within a wider range of grid short-circuit ratios. Finally, simulation and experimental results, which validate the approach, are presented.

Keywords: Grid-forming converters, control-loop interaction, robust control design, small-signal stability, grid connection

1 Introduction

Voltage-source converters (VSCs) have become more predominant in modern power systems as the penetration of renewable energy sources increases [1]. In general, these VSCs operate in the grid-following mode or grid-forming mode [2]. Grid-following VSCs feed the power to the grid via the vector current control, which is synchronized with the voltage at the point of connection (PoC) [3]. Grid-forming VSCs regulate output voltages and achieve synchronization with the grid based on the injected power [4].

However, when interacting with grid impedances, both control schemes can suffer from control interaction problems, leading to small-signal instability [5]. Grid-following VSCs tend to be unstable when operating in weak grids with low short-circuit capability [6-8]. The problem has been extensively studied [9-11], and the negative resistance caused by the phase-locked loop (PLL) is found as the major root cause [9]. The

robustness of grid-following VSCs can thus be improved by reducing the PLL bandwidth (BW).

In contrast, grid-forming VSCs are prone to oscillate in stiff grids [12]. In recent years, the problem has been increasingly noticed and studied based on the small-signal stability analysis. Existing methods for analyzing this problem can be classified into two categories: ① state-space eigenvalue analysis and ② impedance-based stability analysis.

The state-space eigenvalue analysis, also named as modal analysis, analyzes the eigenvalues of the system state matrix based on the time-domain state-space model. Then, participation factor [13] and parameter sensitivity analysis can be utilized to evaluate how state variables and control parameters affect the overall system stability [14]. The stability of grid-forming VSCs has been shown affected by many factors, including the droop control coefficient [15], voltage control (VC) [13, 16], and system operating point [17]. Although the state-space model can accurately characterize the overall system dynamics, the analysis result only applies to a specific grid condition. Its modeling and analysis have to be

repeated if the grid condition is changed. Therefore, the adverse effects of VSC control loops on the VSC-grid interaction explained in terms of the VSC terminal dynamics remain unknown.

To resolve this problem, the impedance-based stability analysis has been adopted to analyze the VSC-grid interaction. In this approach, the entire system is partitioned at the PoC of the VSC, where the small-signal VSC impedance and grid impedance are modeled separately to characterize the voltage-current relationships viewed from each side [18]. Then, the system stability can be analyzed in two ways: ① passivity-based analysis of the VSC impedance and ② the Nyquist stability criterion (NSC) applied to the minor loop gain formed by the VSC and grid impedances.

The passivity-based analysis provides a sufficient condition for the system stability, i.e., the VSC-grid interaction is stable if each subsystem is stable and passive [19]. The non-passive (or non-dissipative) behavior induced by VSC controls can destabilize VSC-grid interactions. Several works have analyzed the passivity of grid-forming VSCs. The various impacts of voltage controllers on passivity are compared in Ref. [20]; however, this analysis merely focuses on high-frequency stability. The detrimental impact of the voltage feedforward loop on the grid-forming VSC impedance has also been identified in the low-frequency range. This effect can destabilize the system in stiff grids [21]; however, this work ignores the dynamic impacts of the outer-loop power control. Thus, the analysis is inadequate to reveal the low-frequency instability mechanism of grid-forming VSCs.

The NSC-based analysis can accurately predict the system stability based on the VSC and grid impedance models [22-27]. Such analyses characterize the entire control dynamics of the VSC into its output impedance. However, its multi-input multi-output (MIMO) nature requires applying the generalized NSC for the stability analysis [27] or a simplified single-input single-output (SISO) impedance-based stability analysis considering interaction with the grid [26]. The former applies the analysis by calculating the eigenvalue transfer functions of the minor-loop gain matrix, and the latter relies on deriving an equivalent SISO model. Both

analyses lose the physical meaning of the VSC impedance itself. Consequently, they can barely explain how VSC control loops affect impedance shaping and why they can affect the VSC-grid interaction. Because of the lack of these insights, developing a holistic design for improving the stability of a multi-loop control system of a grid-forming VSC is difficult.

To resolve these challenges using existing impedance-based stability analysis methods, this paper proposes a control-loop decomposition approach for grid-forming VSCs. The proposed method can characterize the multiple-loop control impacts of grid-forming VSCs using series impedance models, resulting in a design-oriented analysis for VSC-grid interaction.

The remainder of the paper is organized as follows. Section 2 proposes the control-loop decomposition approach for grid-forming VSCs. Section 3 elucidates the use of the proposed approach for robust controller design. Section 4 presents the validation via simulations and experiments. Section 5 finally concludes the paper.

2   Control-loop decomposition

The control-loop decomposition approach is developed for grid-forming VSCs based on small-signal impedance modeling.

2.1   System descriptions and modeling assumptions

To improve clarity, this work assumes a droop-controlled VSC because it is one of the typical grid-forming control schemes [28]. However, the modeling and analysis principles apply to different grid-forming control schemes because the model is derived by transfer functions.

The studied three-phase grid-forming VSC is shown in Fig. 1 with a single-line representation connected to a grid through the grid impedance, L_g. The power control adopts the droop control with low-pass filters (LPFs). The VC adopts the capacitor-voltage and inductor-current dual-loop control [29]. All circuit and control parameters are listed in Tabs. 1 and 2. In subsequent studies, the converter filter parameters are fixed. Moreover, the stability is analyzed by modifying the control parameters because in practice, designing the control

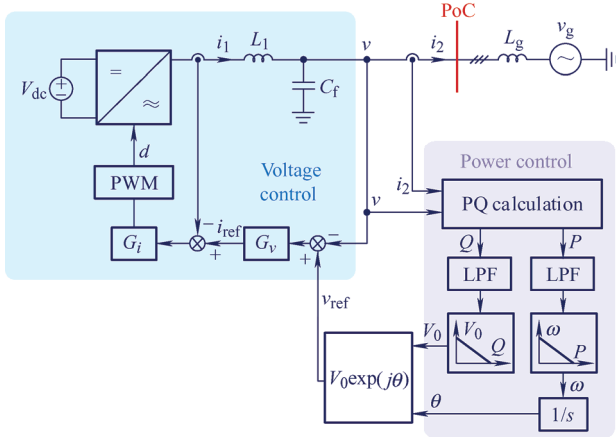of converters is more flexible and cost-effective than designing passive filters.

Fig. 1   Grid-connected grid-forming VSC with droop-based power control and dual-loop VC

Tab. 1   Circuit parameters

Variable	Value
Grid voltage (line to line) V_g/V	190
Nominal fundamental frequency $f_0(\omega_0)$	50 Hz (2π·50 rad/s)
LC filter inductance L_1/mH	2
LC filter capacitance C_f/μF	10
Grid inductance L_g/mH	6
Short circuit ratio SCR	10

Tab. 2   VSC control parameters

Variable	Value
Fundamental frequency $f_1(\omega_1)$	50 Hz (2π·50 rad/s)
Switching/sampling frequency f_s/kHz	10
LPF cut-off frequency $f_c(\omega_c)$	1 Hz (2π·1 rad/s)
Rated power P_0, Q_0	2 kW, 2 kVar
Power reference P_{ref}, Q_{ref}	2 kW, 0 Var
Rated voltage reference V_{ref}/V	190
Active power droop coefficient m_P	2%ω_0/P_0
Reactive power droop coefficient n_Q	10%V_{ref}/Q_0
Current controller P gain K_{pi}/Ω	7
Voltage controller P gain K_{pv}/ S	0.01
Voltage controller R gain K_{rv}	50 S/s / 150 S/s
Voltage control bandwidth BW	57 Hz / 167 Hz

2.2   VSC modeling

The frequency-domain model of the grid-forming VSC can be derived in the $\alpha\beta$ frame, which yields the closed-loop model shown in Fig. 2 [26]. The modeling follows two steps.

First, by modeling the inner-loop VC, the VC output impedance matrix can be derived as $\mathbf{Z}_o$, and the voltage-loop closed-loop transfer function matrix can be derived as $\mathbf{G}_{vv}$.

Then, the dynamic modeling of the outer-loop power control is considered. Because the power (PQ) calculation and voltage reference generation are nonlinear, $\mathbf{Z}_{ref}$ and $\mathbf{G}_{ref}$ can be derived through linearization to characterize the input-output relationships from the VSC's output current and output voltage to the voltage reference, respectively.
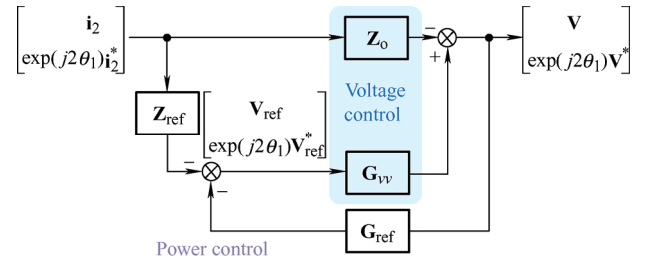

Fig. 2   Closed-loop $\alpha\beta$-frame model of grid-forming VSC [26]

The detailed modeling process has been reported in Ref. [26]; the explicit expressions of these frequency-domain transfer function matrices are simply listed as Appendixes in Sections 5.1 and 5.2.

The output impedance model of the VSC observed at the PoC in Fig. 1 can be used to analyze the VSC-grid interaction, which is derived according to Fig. 2 as

$$\begin{bmatrix} \mathbf{v} \\ \exp(j2\theta_1)\mathbf{v}^* \end{bmatrix} = -\mathbf{Z}_{VSC} \begin{bmatrix} \mathbf{i}_2 \\ \exp(j2\theta_1)\mathbf{i}_2^* \end{bmatrix}$$

where

$$\mathbf{Z}_{VSC} = \left(\mathbf{I} + \mathbf{G}_{vv}\mathbf{G}_{ref} \right)^{-1} \left(\mathbf{Z}_o + \mathbf{G}_{vv}\mathbf{Z}_{ref} \right) \qquad (1)$$

2.3   Control-loop decomposition

If the VSC impedance model is entirely derived, then revealing the impacts of different control loops for a design-oriented analysis is difficult. To overcome this challenge, the model shown in Fig. 2 can be further decomposed in forward paths based on the transfer functions of different control loops. In the forward path, $\mathbf{Z}_{ref}$ is further decomposed into $\mathbf{Z}_{refP}$ and $\mathbf{Z}_{refQ}$ based on the active and reactive power transfer functions, respectively.

The control diagram after decomposition is shown in Fig. 3a, where VC, APC, and RPC denote the voltage control, active power control, and reactive power control, respectively. The figure indicates that $(\mathbf{I}+\mathbf{G}_{vv}\mathbf{G}_{ref})^{-1}$ is a common factor in the three forward paths that does not result in any distinctions. Although $\mathbf{G}_{vv}$ appears in the forward paths of APC and RPC, it can be approximated as an identity matrix, $\mathbf{I}$, within the VC BW. Therefore, the major difference in representing the VSC output impedance originates from transfer function matrices, $\mathbf{Z}_o$, $\mathbf{Z}_{refP}$, and $\mathbf{Z}_{refQ}$, which are given as

$$\mathbf{Z}_o = \begin{bmatrix} Z_o(s) & 0 \\ 0 & Z_o(s-j2\omega_1) \end{bmatrix} \tag{2}$$

$$\mathbf{Z}_{refP} = \frac{j}{2}\begin{bmatrix} -V_0 G_P(s-j\omega_1)V_{dq}^* & -V_0 G_P(s-j\omega_1)V_{dq} \\ V_0 G_P(s-j\omega_1)V_{dq}^* & V_0 G_P(s-j\omega_1)V_{dq} \end{bmatrix} \tag{3}$$

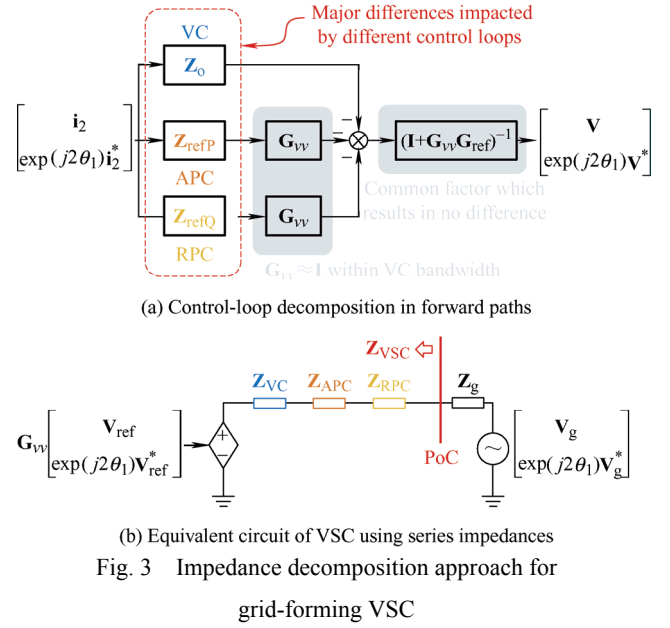$$\mathbf{Z}_{refQ} = \frac{j}{2}\begin{bmatrix} -G_Q(s-j\omega_1)V_{dq}^* & G_Q(s-j\omega_1)V_{dq} \\ -G_Q(s-j\omega_1)V_{dq}^* & G_Q(s-j\omega_1)V_{dq} \end{bmatrix} \tag{4}$$

where $Z_o(s)$ is the SISO output impedance of VC given by Eq. (A9); $G_P(s)$ denotes the transfer function of APC given by Eq. (A12); $G_Q(s)$ represents the transfer function of RPC given by Eq. (A13); V_0 is the steady-state voltage magnitude; and V_{dq} is the complex-valued steady-state voltage aligned with the voltage dq frame, which is equal to V_0 because $V_d = V_0$ and $V_q = 0$.

The control-loop decomposition allows for characterizing the VSC output impedance using several impedances in series, i.e.

$$\mathbf{Z}_{VSC} = \underbrace{(\mathbf{I}+\mathbf{G}_{vv}\mathbf{G}_{ref})^{-1}\mathbf{Z}_o}_{\mathbf{Z}_{VC}} + \underbrace{(\mathbf{I}+\mathbf{G}_{vv}\mathbf{G}_{ref})^{-1}\mathbf{G}_{vv}\mathbf{Z}_{refP}}_{\mathbf{Z}_{APC}} + \underbrace{(\mathbf{I}+\mathbf{G}_{vv}\mathbf{G}_{ref})^{-1}\mathbf{G}_{vv}\mathbf{Z}_{refQ}}_{\mathbf{Z}_{RPC}} \tag{5}$$

where each impedance represents the dynamic impact of each forward path. Then, by decomposing different control loops, the equivalent circuit of the grid-forming VSC is obtained, as shown in Fig. 3b. Accordingly, the impacts of the control loops on VSC impedance shaping can be directly compared and studied on Bode diagrams, benefitting the design-oriented analysis for VSC-grid interaction.

(a) Control-loop decomposition in forward paths

(b) Equivalent circuit of VSC using series impedances

Fig. 3   Impedance decomposition approach for grid-forming VSC

3   Design-oriented analysis

This section presents the conduct of a design-oriented analysis based on the proposed control-loop decomposition approach for the grid-forming VSC. The VSC-grid interaction is studied based on the system shown in Fig. 1.

The flowchart of the design-oriented analysis is shown in Fig. 4. First, the impedance-based stability analysis based on the generalized NSC is implemented for a preliminary stability assessment, which is the existing solution for the impedance-based stability assessment. Then, the VSC-grid interaction is studied by decomposing the VSC and grid impedances based on singular-value analysis, which reveals how VSC
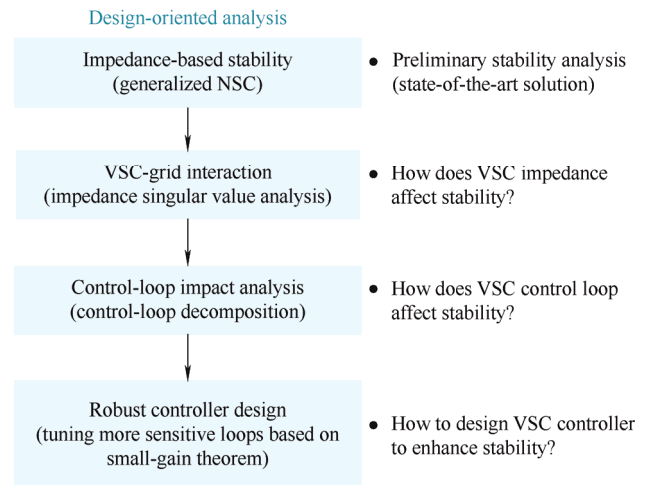

Fig. 4   Flowchart of design-oriented analysis for grid-forming VSC

Yicheng Liao et al.: Controller Design-oriented Analysis of Grid-forming Converters for Stability
Robustness Enhancement

41

impedance affects stability. Next, control-loop decomposition is further conducted to analyze how a specific control loop affects stability. Finally, by implementing the control-loop interaction analysis, a robust controller design based on the small-gain theorem is conducted to enhance stability.

3.1 Impedance-based stability

The VSC-grid interconnected system shown in Fig. 1 can be represented by a closed-loop system using impedance models, as shown in Fig. 5, where the system return ratio is defined as

$$\mathbf{L}(s) = \mathbf{Z}_{VSC}(s)\mathbf{Z}_g^{-1}(s) \tag{6}$$

Then, system stability can be analyzed by applying the generalized NSC to $\mathbf{L}(s)$ [30], where the two eigenvalue transfer functions of $\mathbf{L}(s)$ have to be analyzed by the NSC. Because $\mathbf{Z}_g(s)$ is passive, the phase crossings over 180° of the eigenvalues of $\mathbf{L}(s)$ must be present in the non-passive frequency bands of $\mathbf{Z}_{VSC}(s)$ [31]. Consequently, the stability analysis with the generalized NSC can be simply focused on the non-passive frequency bands of $\mathbf{Z}_{VSC}(s)$.
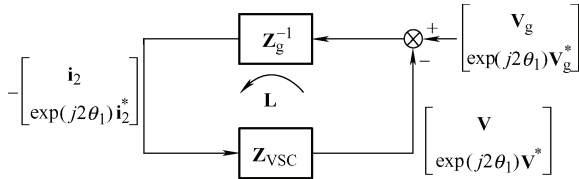

Fig. 5   Representation of VSC-grid interconnected system using impedance models

The passivity of $\mathbf{Z}_{VSC}$ can be checked by the positive realness of the passivity index [32], which is the minimum eigenvalue of the Hermitian part of $\mathbf{Z}_{VSC}$, i.e.

$$p_{min}(\omega) = \min \lambda \left\{ \frac{1}{2}\left(\mathbf{Z}_{VSC}(j\omega) + \mathbf{Z}_{VSC}^{H}(j\omega)\right) \right\} \tag{7}$$

Combining the Bode diagrams of the eigenvalue transfer functions of $\mathbf{L}$ and passivity index of $\mathbf{Z}_{VSC}$, the stability of the grid-forming VSC under a critically unstable case (referred to as Case A) is first studied; here, the grid short-circuit ratio (SCR) is equal to 10. The Bode diagrams of the eigenvalue transfer functions of $\mathbf{L}$ and passivity index of $\mathbf{Z}_{VSC}$ are plotted in Fig. 6. Three non-passive frequency bands of $\mathbf{Z}_{VSC}$, which are in the vicinities of −50 Hz, 50 Hz and 150 Hz, are shown in Fig. 6a. The figure shows that in the

two non-passive frequency bands in the vicinities of −50 Hz and 150 Hz, λ_1 and λ_2 do not cross over ±180° . Therefore, the stability analysis can be simply focused on the non-passive frequency band in the vicinity of the fundamental frequency, which is shown in the magnified plot in Fig. 6b.
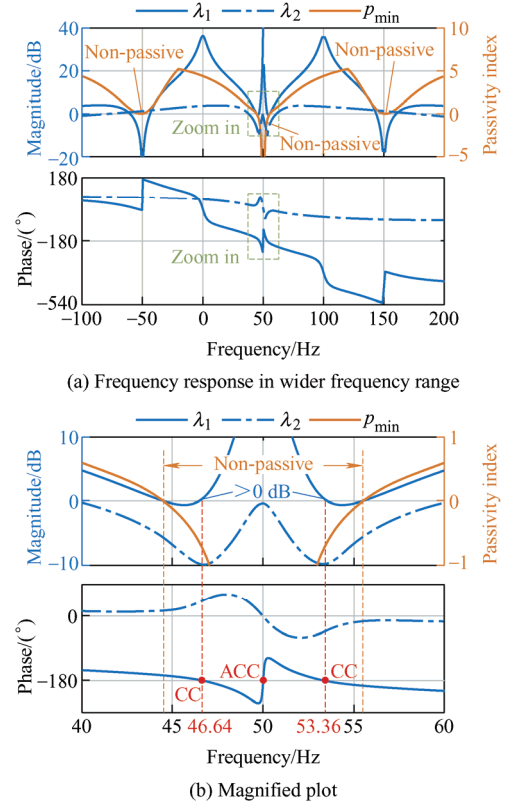

(a) Frequency response in wider frequency range

(b) Magnified plot

Fig. 6   Bode diagrams of eigenvalue transfer functions of $\mathbf{L}$ and passivity index of $\mathbf{Z}_{VSC}$ for Case A

The NSC can then be applied to Fig. 6b. From the Bode diagram of λ_1, a right-half-plane (RHP) pole is identified at 50 Hz because the phase increases at the resonant peak [33]. This RHP pole is actually induced by $(\mathbf{I}+\mathbf{G}_{vv}\mathbf{G}_{ref})^{-1}$ in Eq. (1). Note that the existence of RHP poles does not violate the fact that the grid-forming VSC must be open-circuit stable. This is because in the open-circuit case, the operating current in the VSC is $I_{2dq} = 0$ such that $(\mathbf{I}+\mathbf{G}_{vv}\mathbf{G}_{ref})^{-1} = \mathbf{I}$ according to the expression of $\mathbf{G}_{ref}$ in Eq. (A14). This implies that the existence of RHP poles in the grid-forming VSC impedance is dependent on VSC operating points. From the phase response of λ_1 in the non-passive frequency band, two clockwise crossings (CCs) and one anti-clockwise crossing (ACC) over −180° are observed. The ACC compensates for the impact of the RHP pole; thus, it does not affect

stability. For the two CCs, the corresponding magnitude responses are found to be both critically larger than 0 dB, indicating a critically unstable system.

Notably, the non-passive frequency band for grid-forming VSCs is narrow in the vicinity of the fundamental frequency [34]; this can limit the variation range of potentially unstable oscillation modes.

3.2 VSC-grid interaction

The stability analysis based on the generalized NSC requires the calculation of the eigenvalue transfer functions of $\mathbf{L}$; however, this barely elucidates how the VSC interacts with the grid. To interpret the VSC-grid interaction, singular-value analysis is further conducted by decomposing the VSC and grid impedance models. The eigenvalue of $\mathbf{L}$ is known to be bounded by its maximum singular value, which yields

$$\left| \lambda_i (\mathbf{L}) \right| \leqslant \overline{\sigma} (\mathbf{Z}_{\mathrm{VSC}}) \overline{\sigma} (\mathbf{Z}_{\mathrm{g}}^{-1}) = \overline{\sigma} (\mathbf{Z}_{\mathrm{VSC}}) / \underline{\sigma} (\mathbf{Z}_{\mathrm{g}}) \quad (8)$$

where $\overline{\sigma}(\cdot)$ and $\underline{\sigma}(\cdot)$ denote the maximum and minimum singular values, respectively.

The singular-value analysis of the VSC and grid impedances is shown in Fig. 7. At the phase crossover frequencies (i.e., 46.64 Hz and 53.36 Hz), $\overline{\sigma}(\mathbf{Z}_{\mathrm{VSC}}) / \underline{\sigma}(\mathbf{Z}_{\mathrm{g}}) > 1$, which violates the small-gain theorem [31]; thus, the VSC-grid interaction tends to be unstable. By comparing $\overline{\sigma}(\mathbf{Z}_{\mathrm{VSC}})$ in Fig. 7 and λ_1 in Fig. 6b, the high gain of λ_1 in the vicinity of the fundamental frequency is found to be significantly contributed by the high gain of $\overline{\sigma}(\mathbf{Z}_{\mathrm{VSC}})$. This implies that the considerable magnitude of VSC impedance significantly contributes to instability.
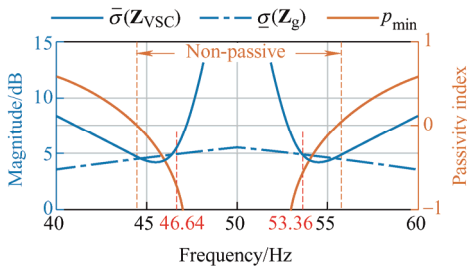

Fig. 7   Singular-value analysis of VSC and grid impedances for Case A

3.3 Control-loop impact analysis

To further analyze how different control loops

affect the impedance shaping of VSC, control-loop decomposition is conducted. According to Eq. (5), the various control-loop effects can be determined by comparing $\mathbf{Z}_{\mathrm{o}}$, $\mathbf{Z}_{\mathrm{refP}}\mathbf{G}_{vv}$, and $\mathbf{Z}_{\mathrm{refQ}}\mathbf{G}_{vv}$; the Bode diagrams are shown in Fig. 8.
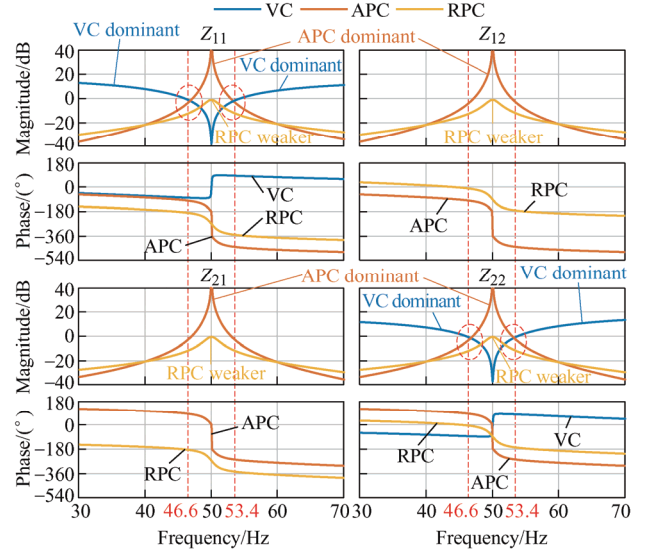

Fig. 8   Bode diagrams of $\mathbf{Z}_{\mathrm{o}}$, $\mathbf{Z}_{\mathrm{refP}}\mathbf{G}_{vv}$, and $\mathbf{Z}_{\mathrm{refQ}}\mathbf{G}_{vv}$

Based on the magnitude comparison in Fig. 8, the APC is observed to be dominant when 50 Hz is approached. When distant from 50 Hz, the VC is dominant. In the frequency range shown in the dashed ellipse, which is in the vicinity of unstable oscillation modes, the impact of RPC is much weaker although those of APC and VC are comparable. These findings indicate that the unstable oscillation mode is more sensitive to APC and VC and less sensitive to RPC.

3.4 Robust control design

Based on the VSC-grid interaction analysis (Fig. 7) and control-loop impact analysis (Fig. 8), robust control design can be further conducted to enhance the system stability according to the following principles.

(1) Based on the small-gain theorem, stability can be enhanced by tuning the controllers to reduce the VSC impedance magnitude that is in the vicinity of the fundamental frequency.

(2) Stability can be improved more effectively by tuning sensitive control loops, such as the VC and APC, as presented in Section 3.3.

To   achieve   a   robust   control   design,

Yicheng Liao et al.: Controller Design-oriented Analysis of Grid-forming Converters for Stability
Robustness Enhancement

43

comprehending how different control loops affect the VSC impedance gain is necessary. The impacts of VC, APC, and RPC can be further investigated based on analytical modeling.

3.4.1 VC impact and design

The diagonal elements of $\mathbf{Z}_o$ (determined by $Z_o(s)$) are derived from the VC output impedance given by Eq. (A9). Due to the closed-loop effect of VC, $Z_o(s)$ exhibits a low impedance value at the fundamental frequency. The relationship of Z_o and VC loop gain (T_v) with respect to the change in VC BW is shown in Fig. 9. With a wider frequency range of $|T_v|>0$ dB, the BW of the VC loop is higher. As the VC-loop BW increases, the magnitude of Z_o can be reduced in the vicinity of the fundamental frequency. A smaller Z_o can thus reduce the magnitude of $\mathbf{Z}_{VSC}$ in the vicinity of the fundamental frequency; this implies that increasing the VC-loop BW can enhance the stability of the grid-forming VSC.
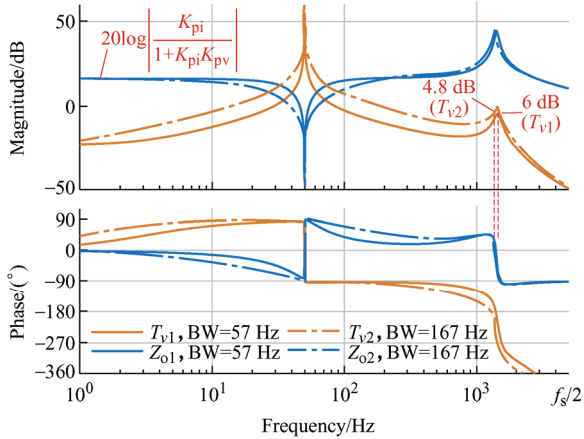

Fig. 9   Bode diagrams of VC loop gains and
VC output impedances

3.4.2 APC impact and design

The impact of APC is mainly contributed by $\mathbf{Z}_{refP}\mathbf{G}_{vv}$. At values close to the fundamental frequency, $\mathbf{G}_{vv}$ can be approximated as an identity matrix due to the effect of voltage closed-loop control. Based on Eq. (3), the impact of APC can be approximately analyzed using $\mathbf{Z}_{refP}$.

Because $V_{dq} = V_0$ under the steady state, the magnitude responses of all elements in $\mathbf{Z}_{refP}$ are the same; they can be analyzed by

$$\left| V_0^2 G_P \left(j\omega - j\omega_1 \right) \right| = \left| m_P V_0^2 \cdot \underbrace{\frac{\omega_c}{j\omega - j\omega_1 + \omega_c}}_{\text{LPF}} \cdot \underbrace{\frac{1}{j\omega - j\omega_1}}_{\text{integrator}} \right| \quad (9)$$

Because G_P is related to the transfer function of APC, the infinite gain in APC impedance at the fundamental frequency (Fig. 8) is found to be contributed by the integrator used in the APC loop. This high gain at the fundamental frequency is inevitable. However, the APC impedance magnitude in the vicinity of the fundamental frequency can still be effectively reduced if the droop coefficient of the APC can be reduced, benefitting the robust controller design of the grid-forming VSC.

3.4.3 RPC impact and design

The impact of RPC is mainly contributed by $\mathbf{Z}_{refQ}\mathbf{G}_{vv}$. Similarly, it can be approximately analyzed by $\mathbf{Z}_{refQ}$ in the vicinity of the fundamental frequency according to Eq. (4).

The magnitude responses of all elements in $\mathbf{Z}_{refQ}$ can be analyzed by

$$\left| V_0 G_Q \left(j\omega - j\omega_1 \right) \right| = \left| n_Q V_0 \cdot \underbrace{\frac{\omega_c}{j\omega - j\omega_1 + \omega_c}}_{\text{LPF}} \right| \quad (10)$$

Because the RPC only adopts droop control, it does not result in infinite gain at the fundamental frequency. As it approaches the fundamental frequency, its impact becomes less significant compared with that of the APC. The impact of RPC can be more significant than that of APC when it is distant from the fundamental frequency; nevertheless, its impact remains considerably weaker compared with that of VC. Similarly, reducing the RPC's droop coefficient can also diminish the RPC-loop impact. However, tuning the RPC loop is less contributive compared with tuning the VC or APC loop. Thus, in this case, tuning the RPC loop is unnecessary for improving the stability robustness.

4   Validation

This section presents the validation of the robust control design (Section 3) through stability analyses, simulations, and experiments.

The experimental setup is shown in Fig. 10. A grid simulator (Chroma 61845) is used to generate an ideal three-phase voltage source. The VSC is fed by a direct-current source, and the control is implemented in dSPACE (DS1007). The circuit parameters and VSC control parameters are the same as those summarized in Tabs. 1 and 2.
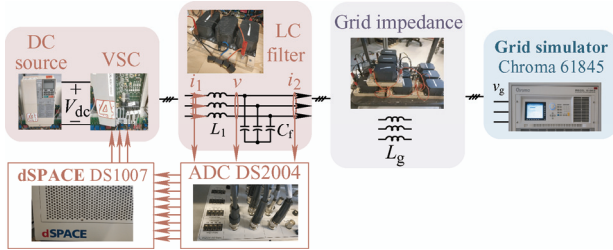

Fig. 10   Experimental setup of grid-connected grid-forming VSC

4.1   Experimental validation of Case A

The stability analysis of Case A, which is critically unstable, is presented in Fig. 6. First, its experimental validation is conducted; waveforms are shown in Fig. 11. The system is found to be critically unstable with sideband oscillations observed in voltage and current waveforms. Through discrete Fourier transformation (DFT) analysis, the oscillation frequency in the power waveforms is identified as 3.3 Hz. In the $\alpha\beta$ frame, this results in frequencies of 46.7 Hz and 53.3 Hz. Thus, the oscillation frequencies are well predicted by the analysis shown in Fig. 6.
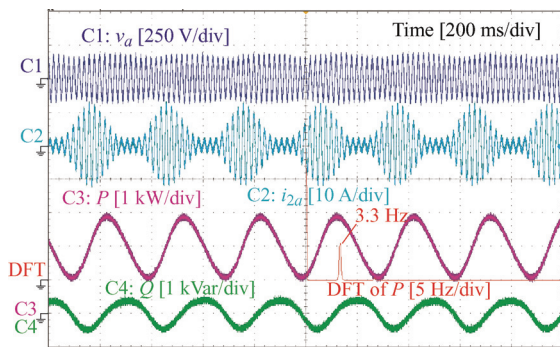

Fig. 11   Experimental waveforms for Case A
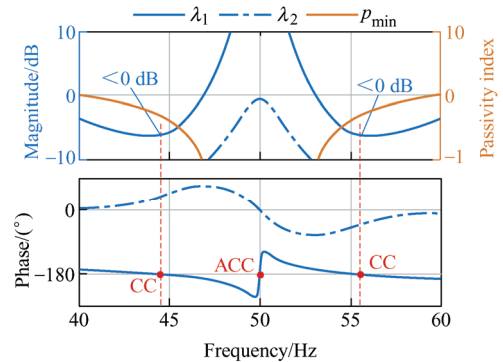
4.2   Robust control design validation

To validate the robust control design presented in Section 3.4, Cases B-D are compared with Case A; these are listed in Tab. 3. Case B studies the impact of VC-loop BW; Case C examines the impact of the APC droop coefficient; Case D investigates the impact of the RPC droop coefficient.
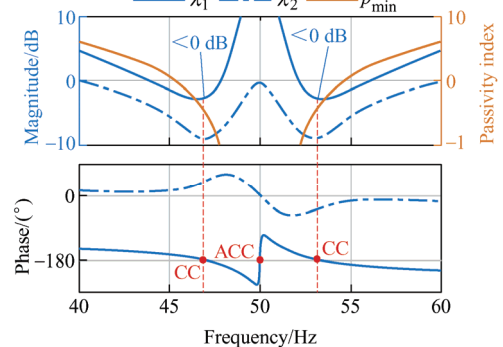
Tab. 3   Case studies

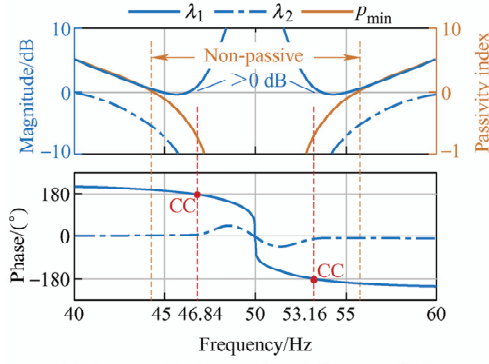| Cases	VC BW/Hz	APC m_p	RPC n_q
A	57	2%ω_0/P_0	10%V_{ref}/Q_0
B	167	2%ω_0/P_0	10%V_{ref}/Q_0
C	57	1%ω_0/P_0	10%V_{ref}/Q_0
D	57	2%ω_0/P_0	1%V_{ref}/Q_0

The stability analyses with the generalized NSC for Cases B-D are shown in Fig. 12. The results can be compared with those of Case A shown in Fig. 6b. As shown in Figs. 12a-12b, by increasing the VC-loop BW or decreasing the APC droop coefficient, system stability can be effectively improved because at the CCs, $|\lambda_1|<0$ dB. This supports the previous control-loop impact analysis that stability is sensitive to VC and APC. As for the RPC loop, even if the RPC droop coefficient is reduced to a tenth of its original value, the system remains critically unstable, as shown in Fig. 12c; note that $|\lambda_1|$ remains greater than 0 dB at the CCs. This proves that stability is not sensitive to the RPC.
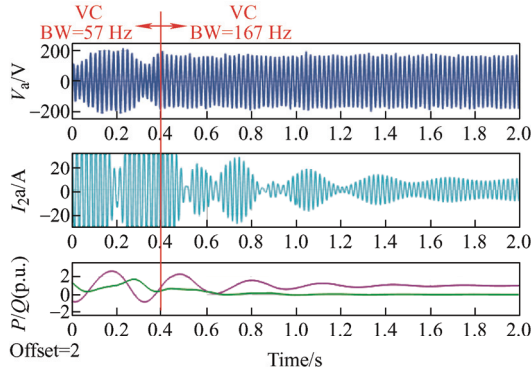

(a) Case B with increased VC BW

(b) Case C with decreased APC droop coefficient

Yicheng Liao et al.: Controller Design-oriented Analysis of Grid-forming Converters for Stability
Robustness Enhancement

45

(c) Case D with decreased RPC droop coefficient
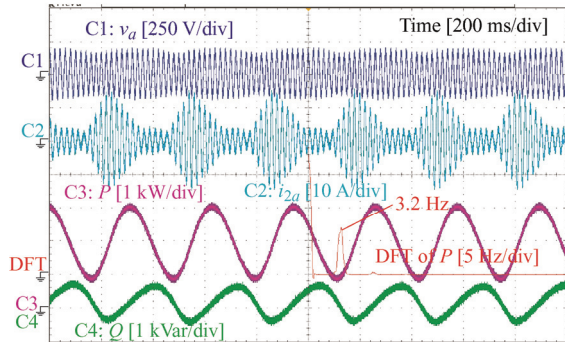
Fig. 12   Stability analysis for Cases B-D

The time-domain validations for Cases B-D are provided in Fig. 13. As shown in Figs. 13a and 13b, increasing the VC BW and reducing the APC droop coefficient can significantly improve the stability of grid-forming VSC. By contrast, Fig. 13c suggests that

(a) Case B with increased VC BW
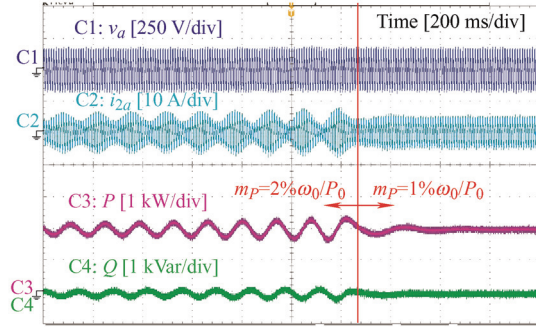
(b) Case C with decreased APC droop coefficient

(c) Case D with decreased RPC droop coefficient

Fig. 13   Simulation and experimental waveforms for Cases B-D the theoretical analysis

tuning the RPC practically does not affect the stability. The simulations and experiments also verify the theoretical analysis.

5   Conclusions and appendixes

A control-loop decomposition approach has been proposed for grid-forming VSCs to study the VSC-grid interaction. Based on the approach, the impacts of VC, APC, and RPC on the stability of a droop-controlled grid-forming VSC in a stiff grid have been studied. The following findings can be summarized as follow.

(1) A low VC-loop BW and the integrator used in the APC can yield high VSC impedance magnitude in the vicinity of the fundamental frequency, which tends to destabilize the VSC-grid interaction.

(2) The instability of the VSC in stiff grids is more sensitive to the VC and APC; however, it is less sensitive to RPC.

Based on the above findings, the robust controller design by tuning the VC and APC using the small-gain theorem has been conducted, widening the range of grid SCRs for the VSC to operate with. Finally, the effectiveness of the control design has been validated by stability analyses, simulations, and experiments.

5.1   Appendix: VC-loop modeling

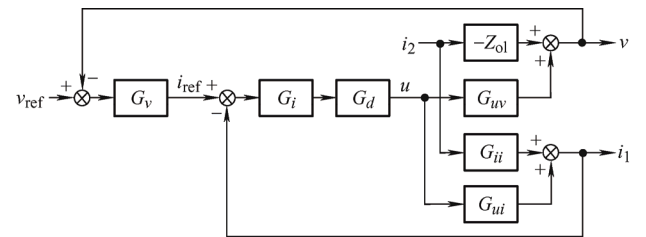The small-signal model of the VC loop is presented in Fig. 14.

Fig. 14   Small-signal model of inner-loop VC [20]

The plant models are

$$Z_{ol} = \frac{Z_{L1}}{1 + Z_{L1}Y_{Cf}} \tag{A1}$$

$$G_{uv} = \frac{1}{1 + Z_{L1}Y_{Cf}} \tag{A2}$$

$$G_{ii} = \frac{1}{1 + Z_{L1}Y_{Cf}} \tag{A3}$$

$$G_{ui} = \frac{Y_{Cf}}{1 + Z_{L1}Y_{Cf}} \tag{A4}$$

The current controller is

$$G_i = K_{pi} \tag{A5}$$

and the voltage controller is

$$G_v = K_{pv} + \frac{K_{rv}s}{s^2 + \omega_1^2} \tag{A6}$$

The time delay is

$$G_d = \exp(-sT_d) = \exp(-1.5sT_s) \tag{A7}$$

The voltage closed-loop transfer function is

$$G_{vv} = \frac{v}{v_{ref}} = \frac{G_{uv}G_dG_iG_v}{1 + G_{ui}G_dG_i + G_{uv}G_dG_iG_v} \tag{A8}$$

The voltage control output impedance is

$$Z_o = -\frac{v}{i_2} = \frac{Z_{ol}(1 + G_{ui}G_dG_i) + G_{uv}G_dG_iG_{ii}}{1 + G_{ui}G_dG_i + G_{uv}G_dG_iG_v} \tag{A9}$$

Note that Eqs. (A8) and (A9) can be similarly derived even if the VC is implemented with different schemes [20]. The SISO models shown in Eqs. (A8) and (A9) require further representation in MIMO forms in the complex-valued $\alpha\beta$ frame, as follows

$$\mathbf{G}_{vv} = \begin{bmatrix} G_{vv}(s) & 0 \\ 0 & G_{vv}(s - j2\omega_1) \end{bmatrix} \tag{A10}$$

$$\mathbf{Z}_o = \begin{bmatrix} Z_o(s) & 0 \\ 0 & Z_o(s - j2\omega_1) \end{bmatrix} \tag{A11}$$

5.2 Appendix: Power control-loop modeling

The active power controller is

$$G_P(s) = -\frac{\omega_c}{s + \omega_c} \cdot \frac{m_P}{s} \tag{A12}$$

and the reactive power controller is

$$G_Q(s) = -\frac{\omega_c}{s + \omega_c} \cdot n_Q \tag{A13}$$

The foregoing equations, Eqs. (A12) and (A13), can also be modified to other transfer functions if different APC and RPC schemes are utilized. In this case, $\mathbf{G}_{ref}$ and $\mathbf{Z}_{ref}$ are linearized small-signal models of power control loops [26]. They are given by

$$\mathbf{G}_{ref}(s) = \frac{j}{2}\begin{bmatrix} G_{ref11} & G_{ref12} \\ G_{ref21} & G_{ref22} \end{bmatrix} \tag{A14}$$

where

$$G_{ref11} = -\left(V_0G_P(s - j\omega_1) - G_Q(s - j\omega_1)\right)I_{2dq}^*;$$
$$G_{ref12} = -\left(V_0G_P(s - j\omega_1) + G_Q(s - j\omega_1)\right)I_{2dq};$$
$$G_{ref21} = \left(V_0G_P(s - j\omega_1) + G_Q(s - j\omega_1)\right)I_{2dq}^*;$$
$$G_{ref22} = \left(V_0G_P(s - j\omega_1) - G_Q(s - j\omega_1)\right)I_{2dq};$$

$I_{2dq} = I_{2d} + jI_{2q}$, which is the steady-state output current.

$$\mathbf{Z}_{ref}(s) = \frac{j}{2}\begin{bmatrix} Z_{ref11} & Z_{ref12} \\ Z_{ref21} & Z_{ref22} \end{bmatrix} \tag{A15}$$

where

$$Z_{ref11} = -\left(V_0G_P(s - j\omega_1) + G_Q(s - j\omega_1)\right)V_{dq}^*;$$
$$Z_{ref12} = -\left(V_0G_P(s - j\omega_1) - G_Q(s - j\omega_1)\right)V_{dq};$$
$$Z_{ref21} = \left(V_0G_P(s - j\omega_1) - G_Q(s - j\omega_1)\right)V_{dq}^*;$$
$$Z_{ref22} = \left(V_0G_P(s - j\omega_1) + G_Q(s - j\omega_1)\right)V_{dq};$$

$V_{dq} = V_d + jV_q$, which is the steady-state output voltage.

References

[1] B Kroposki, B Johnson, Y Zhang, et al. Achieving a 100% renewable grid: Operating electric power systems with extremely high levels of variable renewable energy. *IEEE Power and Energy Mag.*, 2017, 15(2): 61-73.

[2] R H Lasseter, Z Chen, D Pattabiraman. Grid-forming inverters: A critical asset for the power grid. *IEEE J. Emerging Sel. Topics Power Electron.*, 2020, 8(2): 925-935.

[3] J Rocabert, A Luna, F Blaabjerg, et al. Control of power converters in AC microgrids. *IEEE Trans. Power Electron.*, 2012, 27(11): 4734-4749.

[4] L Zhang, L Harnefors, H Nee. Power-synchronization control of grid-connected voltage-source converters. *IEEE Trans. Power Syst.*, 2010, 25(2): 809-820.

[5] X Wang, M G Taul, H Wu, et al. Grid-synchronization stability of converter-based resources: An overview. *IEEE O. J. Ind. Appl.*, 2020, 1: 115-134.

[6] X Wang, F Blaabjerg. Harmonic stability in power electronic based power systems: Concept, modeling, and analysis. *IEEE Trans. Smart Grid*, 2019, 10(3): 2858-2870.

[7] J Z Zhou, H Ding, S Fan, et al. Impact of short-circuit ratio and phase-locked-loop parameters on the small-signal behavior of a VSC-HVDC converter. *IEEE Trans. Power Del.*, 2014, 29(5): 2287-2296.

[8] H Liu, X Xie, J He, et al. Subsynchronous interaction between direct-drive PMSG based wind farms and weak AC networks. *IEEE Trans. Power Syst.*, 2017, 32(6): 4708-4720.

[9] L Harnefors, M Bongiorno, S Lundberg. Input-admittance calculation and shaping for controlled voltage-source converters. *IEEE Trans. Ind. Electron.*, 2007, 54(6): 3323-3334.

[10] B Wen, D Dong, D Boroyevich, et al. Impedance-based analysis of grid-synchronization stability for three-phase paralleled converters. *IEEE Trans. Power Electron.*, 2016,

Yicheng Liao et al.: Controller Design-oriented Analysis of Grid-forming Converters for Stability
Robustness Enhancement

47

31(1): 26-38.

[11] X Wang, L Harnefors, F Blaabjerg. Unified impedance model of grid-connected voltage-source converters. *IEEE Trans. Power Electron.*, 2018, 33(2): 1775-1787.

[12] G Denis, T Prevost, P Panciatici, et al. Improving robustness against grid stiffness, with internal control of an AC voltage-controlled VSC. *in Proc. IEEE Power and Energy Society General Meeting (PESGM)*, 2016, Boston, MA, 2016: 1-5.

[13] T Qoria, F Gruson, F Colas, et al. Analysis of the coupling between the outer and inner control loops of a grid-forming voltage source converter. *in Proc. Europ. Conf. Power Electron. and Appl. (EPE)*, 2020: 1-10.

[14] S D'Arco, J A Suul, O Fosso. Automatic tuning of cascaded controllers for power converters using eigenvalue parametric sensitivities. *IEEE Trans. Ind. Appl.*, 2015, 51(2): 1743-1753.

[15] E Barklund, N Pogaku, M Prodanovic, et al. Energy management in autonomous microgrid using stability-constrained droop control of inverters. *IEEE Trans. Power Electron.*, 2008, 23(5): 2346-2352.

[16] K Yu, Q Ai, S Wang, et al. Analysis and optimization of droop controller for microgrid system based on small-signal dynamic model. *IEEE Trans. Smart Grid*, 2016, 7(2): 695-705.

[17] Y Prabowo, V M Iyer, B Kim, et al. Modeling and stability assessment of single-phase droop controlled solid state transformer. *in Proc. Inter. Conf. on Power Electron. and ECCE Asia*, 2019, Busan, Korea, 2019: 3285-3291.

[18] X Wang, F Blaabjerg, W Wu. Modeling and analysis of harmonic stability in an AC power-electronics-based power system. *IEEE Trans. Power Electron.*, 2014, 29(12): 6421-6432.

[19] L Harnefors, X Wang, A G Yepes, et al. Passivity based stability assessment of grid-connected VSCs: An overview. *IEEE J. Emerging Sel. Topics Power Electron.*, 2016, 4(1): 116-125.

[20] Y Liao, X Wang, F Blaabjerg. Passivity-based analysis and design of linear voltage controllers for voltage-source converters. *IEEE O. J. Ind. Electron. Soc.*, 2020, 1: 114-126.

[21] G Denis. From grid-following to grid-forming: The new strategy to build 100% power electronics interfaced transmission system with enhanced transient behavior. Villeneuve-d'Ascq: Ecole Centrale de Lille, 2017.

[22] S Wang, Z Liu, J Liu, et al. Small-signal modeling and stability prediction of parallel droop-controlled inverters based on terminal characteristics of individual inverters.

[23] W Cao, Y Ma, F Wang, et al. Low-frequency stability analysis of inverter-based islanded multiple-bus AC microgrids based on terminal characteristics. *IEEE Trans. Smart Grid*, 2020, 11(5): 3662-3676.

[24] F Cavazzana, A Khodamoradi, H Abedini, et al. Analysis of an impedance modeling approach for droop-controlled inverters in system DQ frame. *in Proc. IEEE Energy Conversion Congress and Exposition (ECCE)*, 2019, Baltimore, MD, USA, 2019.

[25] W Wu，Y Chen，L Zhou, et al. Sequence impedance modeling and stability comparative analysis of voltage-controlled VSGs and current-controlled VSGs. *IEEE Trans. Ind. Electron.*, 2019, 66(8): 6460-6472.

[26] Y Liao, X Wang, F Liu, et al. Sub-synchronous control interaction in grid-forming VSCs with droop control. *in Proc. IEEE Workshop on the Electronic Grid (eGRID)*, 2019, Xiamen, China, 2019: 1-6.

[27] K Oue, S Sano, T Kato, et al. Stability analysis of grid-forming inverter in DQ frequency domain. *in Proc. IEEE Workshop on Control and Modeling for Power Electronics (COMPEL)*, 2019, Toronto, ON, Canada, Jun. 2019.

[28] S D'Arco, J A Suul. Equivalence of virtual synchronous machines and frequency-droops for converter-based microgrids. *IEEE Trans. Smart Grid*, 2014, 5(1): 394-395.

[29] P C Loh, M J Newman, D N Zmood, et al. A comparative analysis of multiloop voltage regulation strategies for single and three-phase UPS systems. *IEEE Trans. Power Electron.*, 2003, 18(5): 1176-1185.

[30] I Postlethwaite. A generalized inverse Nyquist stability criterion. *Int. J. Control*, 1977, 26(3): 325-340.

[31] J Bao, F Wang, P L Lee, et al. New frequency-domain phase-related properties of MIMO LTI passive systems and robust controller synthesis. *in Proc. 13th World Congr. of IFAC*, 1996, San Francisco, USA, 1996: 3276-3281.

[32] A J Agbemuko, J L Dominguez-Garcia, O Gomis-Bellmunt, et al. Passivity-based analysis and performance enhancement of a vector controlled VSC connected to a weak ac grid. *IEEE Trans. Power Delivery*, 2021, 36(1): 156-167.

[33] Y Liao, X Wang. Impedance-based stability analysis for interconnected converter systems with open-loop RHP poles. *IEEE Trans. Power Electron.*, 2020, 35(4): 4388-4397.

[34] M Bongiorno. Challenges and opportunities in power electronics dominated grids. *in KTH Workshop on Emerging Topics in Control of Power Systems*, 2020.

Yicheng Liao (S'16-M'21) received the B.S. and M.S. degrees in Electrical Engineering from Southwest Jiaotong University, Chengdu, China, in 2015 and 2018, respectively, and the Ph.D. degree in Energy Technology from Aalborg University, Aalborg, Denmark, in 2021.

She was a Visiting Student with Ecole Polytechnique and French National Institute for Research in Digital Science and Technology, Paris, France, in July 2017. From September 2018 to July 2021, she was with the AAU Energy, Aalborg University, as a Research Assistant and later on a Postdoc. Since August 2021, she has become a Postdoc with the School of Electrical Engineering and Computer Science, KTH Royal Institute of Technology, Stockholm, Sweden. Her research interests include the modeling, stability analysis, and control of power electronics-based power systems.

Dr. Liao was selected as the 2020 Outstanding Reviewer of IEEE Transactions on Power Electronics and the 2020 Star Reviewer of IEEE Journal of Emerging and Selected Topics in Power Electronics. She was the recipient of the 2020 Top Download Paper Award in IEEE Open Journal of the Industrial Electronics Society and the 2021 Ph.D. Thesis Talk Award in IEEE Power Electronics Society.

Xiongfei Wang (S'10-M'13-SM'17) received the B.S. degree from Yanshan University, Qinhuangdao, China, in 2006, the M.S. degree from Harbin Institute of Technology, Harbin, China, in 2008, both in Electrical Engineering, and the Ph.D. degree in Energy Technology from Aalborg University, Aalborg, Denmark, in 2013.

From 2009 he has been with the Department of Energy Technology, Aalborg University, where he became an Assistant Professor in 2014, an Associate Professor in 2016, a Professor and Leader of Electronic Power Grid (eGrid) Research Group in 2018. He is also a Visiting Professor at KTH Royal Institute of Technology, Stockholm, Sweden, from 2020. His current research interests include modeling and control of power electronic converters and systems, stability and power quality of power-electronics-dominated power systems, high-power converters.

Dr. Wang serves as a Member-at-Large of Administrative Committee for the IEEE Power Electronics Society (PELS) in 2020-2022, a Co-Editor-in-Chief for the IEEE Transactions on Power Electronics Letters, and as an Associate Editor for the IEEE Journal of Emerging and Selected Topics in Power Electronics (JESTPE). He was selected into Aalborg University Strategic Talent Management Program in 2016. He has received 6 Prize Paper Awards in the IEEE Transactions and conferences, the 2018 Richard M. Bass Outstanding Young Power Electronics Engineer Award, the 2019 IEEE PELS Sustainable Energy Systems Technical Achievement Award, the 2020 IEEE Power & Energy Society Prize Paper Award, the 2020 JESTPE Star Associate Editor Award, and the Highly Cited Researcher in the Web of Science in 2019-2020.